Symmetry, spin-texture, and tunable quantum geometry in a WTe$_2$ monolayer

Li-kun Shi[1] and Justin C. W. Song[1,2]

[1]*Institute of High Performance Computing, Agency for Science, Technology, & Research, Singapore 138632*
[2]*Division of Physics and Applied Physics, Nanyang Technological University, Singapore 637371*

The spin orientation of electronic wave functions in crystals is an *internal* degree of freedom, typically insensitive to electrical knobs. We argue from a general symmetry analysis and a $\mathbf{k} \cdot \mathbf{p}$ perspective, that monolayer $1T'$-WTe$_2$ possesses a gate-activated canted spin texture that produces an electrically tunable bulk band quantum geometry. In particular, we find that due to its out-of-plane asymmetry, an applied out-of-plane electric field breaks inversion symmetry to induce both in-plane and out-of-plane electric dipoles. These in-turn generate spin-orbit coupling to lift the spin degeneracy and enable a bulk band Berry curvature and magnetic moment distribution to develop. Further, due to its low symmetry, Berry curvature and magnetic moment in $1T'$-WTe$_2$ possess a dipolar distribution in momentum space, and can lead to unconventional effects such as a current induced magnetization and quantum nonlinear anomalous Hall effect. These render $1T'$-WTe$_2$ a rich two-dimensional platform for all-electrical control over quantum geometric effects.

I. INTRODUCTION

Structure and material property/functionality have an intimate relationship. A striking example is monolayer WTe$_2$ where a structural change from $1T$ to a distorted $1T'$ structure induces a topological phase transition from trivial to Z_2 topological phase [1]. Recently realized in experiment [2–4], the distorted $1T'$-WTe$_2$ monolayer possesses a large bulk band gap ~ 0.055 eV [2], and helical edge modes that mediate robust edge conduction [3,4] characteristic of a robust quantum spin Hall state.

Here we argue that, aside from determining the band topology, the distorted crystal structure of $1T'$-WTe$_2$ [Figs. 1(a)–1(c)] also enables unusual bulk band quantum geometry and spin physics to be accessed and controlled. By developing a low-energy $\mathbf{k} \cdot \mathbf{p}$ model from symmetry analysis, we find that when an out-of-plane electric field $E_\perp$ is applied, spin-degeneracy is lifted [Figs. 1(d) and 1(e)] by inducing both in-plane as well as out-of-plane spin orientations [Figs. 2(a) and 2(b)]. While in-plane spin orientations are synonymous with an out-of-plane inversion symmetry (IS) breaking, out-of-plane spin orientations are less common and typically weak [5]. As we discuss, $1T'$-WTe$_2$ bucks this expectation: even though $E_\perp$ is out-of-plane, the nonaligned outer Te atoms [Fig. 1(c)] enable an in-plane electric dipole to develop and a strong out-of-plane spin orientation to be induced.

Crucially, applied $E_\perp$ induces Berry curvature as well as a magnetic moment. The Berry curvature value is determined by an interplay between strong atomic (spin-selective) interorbital mixing of the $1T'$-WTe$_2$ and $E_\perp$ induced terms, and it exhibits a characteristic anisotropic distribution; the magnetic moment mirrors this behavior (see Fig. 6). While an electrically tunable Berry curvature can be readily realized in bilayer systems [6] due to an electric control over layer degrees of freedom, electrical tunability in *monolayer* systems is considerably more difficult. Berry curvature is realizable

in $1T'$-WTe$_2$ as a direct result of the asymmetric nonaligned outer Te atoms.

Further, due to the low symmetry of $1T'$-WTe$_2$ distorted crystal structure, the induced Berry curvature and magnetic moment also possess an asymmetry characterized by a dipolar distribution in reciprocal space. As a result, shifts in the distribution function (e.g., induced when a dissipative charge current is flowing, $\mathbf{j}$) enable a net Berry flux and a net out-of-plane magnetization, M_z, to develop (Fig. 4). The latter corresponds to a direct (linear) magnetoelectric effect $M_z = \sum_i \tilde{\alpha}_{zi} j_i$ ($i = x, y$), where $\tilde{\alpha}_{zi}$ characterizes the strength of the magnetoelectric effect; the former mediates a quantum nonlinear anomalous Hall effect [7].

Both of these are intimately tied to the low symmetry of gated $1T'$-WTe$_2$; they do not appear in rotationally symmetric systems. They constitute striking experimental signatures of the tunable quantum geometry (induced Berry curvature and magnetic moment) of $1T'$-WTe$_2$, as well as the direct impact that its distorted structure has on its material response. Using available parameters for $1T'$-WTe$_2$, we anticipate a sizable M_z that can be readily probed for, e.g., using Kerr effect microscopy [8]. $1T'$-WTe$_2$ provides a compelling venue to manipulate spins and magnetic moments in a tunable two-dimensional material. Out-of-plane spin orientations are particularly useful since they may enable us to couple to out-of-plane spins necessary for high-density magnetic applications [9,10].

II. SYMMETRY ANALYSIS AND k · p MODEL

We begin by analyzing the band structure of monolayer $1T'$-WTe$_2$ in the presence of an applied out-of-plane electric field $E_\perp$ [Fig. 1(a)]. In doing so, we will employ a $\mathbf{k} \cdot \mathbf{p}$ method based on the underlying symmetries of the material for, e.g., mirror symmetry about the xz mirror plane [dashed line in Fig. 1(b)], time-reversal symmetry (TRS), and (broken)
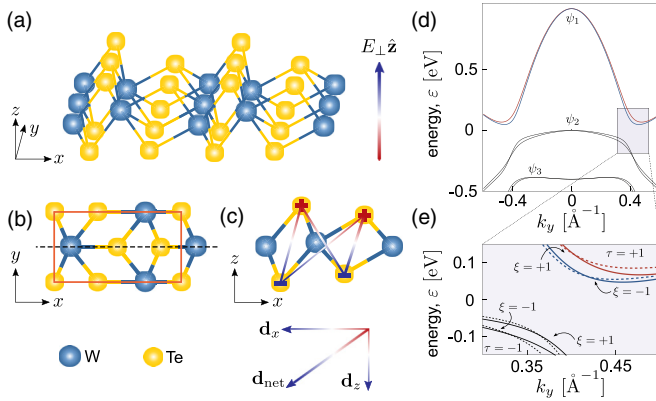
FIG. 1. (a,b) Crystal structure for a $1T'$-WTe$_2$ monolayer possesses a particularly low symmetry with (b) a single mirror plane black dashed line (primitive cell denoted by a red box). (c) A net in-plane dipole moment d_x can be induced by a perpendicular electric field $E_\perp$ as a result of nonalignment of the Te atoms on the top and bottom layers. (d,e) The electronic band structure of a bulk $1T'$-WTe$_2$ monolayer along the k_y direction when a perpendicular electric field is applied possesses [zoom-in, (e)] spin-split conduction and valence bands near the gap opening. Solid and dashed lines are the band structure from the six-band (SBD) and the effective four-band $h^{\text{eff}}(\mathbf{k})$ models, respectively. Parameters used: for the pristine part we used values listed in Table III [11]. For the electric-field-induced part, we used $\alpha_{x,y} = \lambda = \delta_x = 0$, and $\delta_z = 0.025$ eV as an illustration.

inversion symmetry (IS). For completeness, our analysis takes into account the three relevant atomic orbitals ($\psi_{1,2,3}$) and two spin states ($\uparrow, \downarrow$) that contribute to the states near the Γ point and the gap opening [Fig. 1(d)], as revealed by ARPES measurements [2] as well as first-principles calculations [1,12–14]. This produces a six-band $\mathbf{k} \cdot \mathbf{p}$ description (SBD); see the Appendix [11] for a detailed account of the symmetry analysis of these orbitals and spin operators and the symmetry-allowed terms in the SBD description.

Importantly, while $E_\perp = 0$ produces a spin-degenerate band structure [1,2,12–14], when $E_\perp \neq 0$ (e.g., induced by a proximal gate) we find the bands become *spin-split* [Fig. 1(d)]. As shown in Fig. 1(d), this is particularly relevant away from the Γ point, where the splitting becomes pronounced close to the band gap [gray shaded region, Figs. 1(d) and 1(e)]. These are characterized by states $\Psi_{\tau\xi}$ with higher ($\xi = +1$) or lower ($\xi = -1$) energies as shown in Fig. 1(e), and $\tau = \pm 1$ correspond to the conduction and valence bands. As we will see, the splitting induced by $E_\perp$ drives a range of spin behavior.

At low carrier densities typical for $1T'$-WTe$_2$ devices [4], the electronic and spin behavior is dominated by low-energy excitations around the band gap in the four bands [Fig. 1(e)]. To compactly illustrate the physics, we develop a simple effective four-band model using the basis $\{\psi_{c\uparrow}, \psi_{v\uparrow}, \psi_{c\downarrow}, \psi_{v\downarrow}\}$ in the regime around the gap opening (see the gray region). This is obtained by performing a Löwdin partitioning (see [11]) of the bands in Fig. 1(d), and it can be expressed as $h^{\text{eff}}(\mathbf{k}) = h_0(\mathbf{k}) + h_1(\mathbf{k})$. Here $h_0(\mathbf{k})$ describes the electronic

behavior in pristine $1T'$-WTe$_2$ ($E_\perp = 0$):

$$h_0(\mathbf{k}) = \bar{\epsilon}_{\mathbf{k}} + \begin{pmatrix} m_{\mathbf{k}} & v_{\mathbf{k}}^+ & 0 & 0 \\ -v_{\mathbf{k}}^- & -m_{\mathbf{k}} & 0 & 0 \\ 0 & 0 & m_{\mathbf{k}} & v_{\mathbf{k}}^- \\ 0 & 0 & -v_{\mathbf{k}}^+ & -m_{\mathbf{k}} \end{pmatrix}, \quad (1)$$

where $\bar{\epsilon}_{\mathbf{k}} = (\epsilon_{c\mathbf{k}} + \epsilon_{v\mathbf{k}})/2$, $m_{\mathbf{k}} = (\epsilon_{c\mathbf{k}} - \epsilon_{v\mathbf{k}})/2$, and $v_{\mathbf{k}}^\pm = \pm v_x k_x + i v_y k_y$ represents the strong spin-selective atomic orbital coupling (sharing the same spin), while $\epsilon_{c\mathbf{k}}$ and $\epsilon_{v\mathbf{k}}$ are diagonal parts for the conduction and valence bands, capturing their energy offsets and effective masses [11]. We note that $h_0(\mathbf{k})$ is simply a *tilted* Bernevig-Hughes-Zhang (BHZ) Hamiltonian [15] that describes the spin-degenerate bands in pristine $1T'$-WTe$_2$; here the tilt arises from large effective-mass differences between the conduction and valence bands (see Table III [11]).

On the other hand, $h_1(\mathbf{k}) = h_Z(\mathbf{k}) + h_R(\mathbf{k})$ captures the electric-field-induced spin-orbit couplings that are allowed by symmetry,

$$h_Z(\mathbf{k}) = \begin{pmatrix} \lambda k_y & i\delta_z & 0 & 0 \\ -i\delta_z & \lambda k_y & 0 & 0 \\ 0 & 0 & -\lambda k_y & -i\delta_z \\ 0 & 0 & i\delta_z & -\lambda k_y \end{pmatrix},$$

$$h_R(\mathbf{k}) = \begin{pmatrix} 0 & 0 & \alpha_{\mathbf{k}}^- & i\delta_x \\ 0 & 0 & i\delta_x & \alpha_{\mathbf{k}}^- \\ \alpha_{\mathbf{k}}^+ & -i\delta_x & 0 & 0 \\ -i\delta_x & \alpha_{\mathbf{k}}^+ & 0 & 0 \end{pmatrix}, \quad (2)$$

where we have grouped the electric-field-induced spin-orbit coupling terms into $h_Z(\mathbf{k})$ and $h_R(\mathbf{k})$ in order to highlight the out-of-plane and in-plane spin orientations they induce, respectively (see Fig. 2). Here $\alpha_{\mathbf{k}}^\pm = \pm i\alpha_x k_x + \alpha_y k_y$, $\delta_{x,z}$ are k-independent coupling terms, and λk_y is a k-dependent term that can induce out-of-plane spin orientation. We note, parenthetically, that the spin-orbit coupling terms in h_Z have sometimes been referred to as "Zeeman-like," see, e.g., Refs. [5,14], so as to highlight the out-of-plane spin orientation it induces; in the following, we will not use this terminology, but instead focus on their physical manifestation: its spin orientation. We emphasize that both $h_Z(\mathbf{k})$ and $h_R(\mathbf{k})$ in this work physically originate from IS breaking induced by the application of the electric field; see the next section for a detailed discussion.

In writing Eq. (2), we have kept all symmetry-allowed terms up to linear order in k as allowed by symmetry. We remark that the magnitudes of each of the symmetry-allowed terms can be determined from experimental or first-principles calculation results (see the Appendix [11] for a discussion). However, before we move to specific values, we first discuss the physical origin of the coupling terms and some possible interplays brought by these couplings.

III. PHYSICAL ORIGIN OF OUT-OF-PLANE AND IN-PLANE SPIN ORIENTATIONS

For physical clarity, we will denote $h_R(\mathbf{k})$ and $h_Z(\mathbf{k})$ as spin-orbit coupling induced by out-of-plane and in-plane IS breaking, respectively. In a general sense, $h_R(\mathbf{k})$ [or $h_Z(\mathbf{k})$] always couple states with opposite spins (the same spin). As a result, these terms split the spin degeneracy and reorient the spins of the eigenstate $\Psi_{\tau\xi}$: h_R terms create in-plane spin
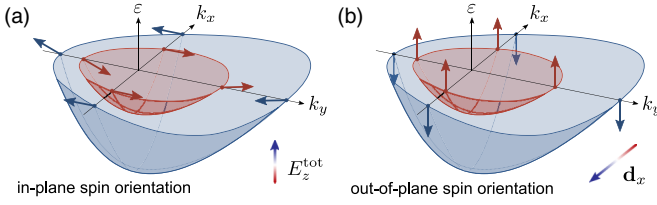
FIG. 2. (a,b) Schematic spin splitting and spin texture of the conduction band (near the gap) induced by an applied electric field. These can be classed as (a) in-plane spin orientation (α, $\delta_x \neq 0$, λ, $\delta_z = 0$) originating from an out-of-plane electric field E_z^{tot}, or (b) out-of-plane spin orientation (α, $\delta_x = 0$, λ, $\delta_z \neq 0$) arising from an in-plane dipole d_x.

orientations [Fig. 2(a)], whereas h_Z terms align spins out-of-plane [Fig. 2(b)]. Here spin orientations are plotted only for the right valley ($k_y > 0$). For $k_y < 0$, spin textures are flipped.

Their physical origins are also distinct. When a charge-neutral monolayer $1T'$-WTe$_2$ is placed under $E_\perp$, the top layer and the bottom layer Te atoms experience a charge redistribution becoming oppositely charged. This charge redistribution counteracts $E_\perp$ forming an out-of-plane dipole moment, d_z [see Fig. 1(c)]. Crucially, because the Te atoms are not perfectly aligned, this charge redistribution also creates an *in-plane* electric dipole moment along the x direction, d_x, yielding a net induced electric dipole, $\mathbf{d}_{\text{net}}$, that is canted [see Fig. 1(c)].

As a result, $E_\perp$ induces IS breaking in *both* z and x directions developing a nonzero $\partial_z \phi(\mathbf{r})$ and $\partial_x \phi(\mathbf{r})$; here $\phi(\mathbf{r})$ is the local electrostatic potential induced by $E_\perp$. Since spin-orbit coupling arises as matrix elements of the microscopic spin-orbit interaction: $\hat{H}_{\text{so}}(\mathbf{k}) \sim (\hbar \mathbf{k} + \hat{\mathbf{p}}) \cdot \mathbf{s} \times \nabla \phi(\mathbf{r})$ (see, e.g., Eq. (16.1) of Ref. [16] or Eq. (2.4) of Ref. [17]), we find that spin-orbit coupling terms δ_x and $\alpha_{\mathbf{k}}^\pm$ come from the total out-of-plane electric field $-\partial_z \phi(\mathbf{r})$; this constrains the terms $\hbar \mathbf{k} + \hat{\mathbf{p}}$ and $\mathbf{s}$ in $\hat{H}_{\text{so}}(\mathbf{k})$ to be in-plane only. However, the charge redistribution also enables an in-plane $\partial_x \phi(\mathbf{r})$ to develop. This in-plane electric field picks out $\mathbf{s}$ in $\hat{H}_{\text{so}}(\mathbf{k})$ as the out-of-plane component s_z, and $\hbar \mathbf{k} + \hat{\mathbf{p}}$ as the y component. As a result of the in-plane $\partial_x \phi(\mathbf{r})$, h_Z terms λk_y and δ_z in Eq. (2) manifest. The *distorted* structure of $1T'$-WTe$_2$ enables $\mathbf{d}_{\text{net}}$ that is generically canted with finite h_Z and h_R terms that coexist. In contrast, since λk_y and δ_z result from the in-plane electric field $\partial_x \phi(\mathbf{r})$, the nondistorted transition-metal dichalcogenide monolayers whose atoms at the top and bottom layers are aligned (e.g., MoS$_2$) do not possess an external $E_\perp$-induced out-of-plane spin orientation near the Γ point (up to linear in k).

As a further illustration of the role that low symmetry plays in $1T'$-WTe$_2$, we can also compare the spin-orbit coupling terms in $h_R(\mathbf{k})$ allowed in $1T'$-WTe$_2$ (induced by out-of-plane IS breaking) with that of HgTe quantum wells recently discussed in the literature [18,19]. For $1T'$-WTe$_2$, all terms in $h_R(\mathbf{k})$ are allowable when an out-of-plane electric field is applied because of its very low symmetry, and the fact that angular momentum in the z direction is not a good quantum number. In contrast, HgTe quantum wells possess a D_{2d} symmetry, $[h_R(\mathbf{k})]_{24,(42)}$ is missing because its second and fourth basis functions are heavy-hole bands with $j_z = \pm 3/2$, and the coupling between them is at least of k^3 order. Only $i\delta_x$

and $[h_R(\mathbf{k})]_{13,(31)}$ can appear, corresponding to the existence of bulk inversion asymmetry [18] and structural inversion asymmetry [19], respectively.

IV. INTERPLAY BETWEEN BERRY CURVATURE AND THE TWO TYPES OF SPIN-ORBIT COUPLINGS

Pristine $1T'$-WTe$_2$ possesses both IS and TRS, ensuring that Berry curvature (and orbital magnetic moment) vanishes exactly. As we now discuss, in $1T'$-WTe$_2$ with $E_\perp \neq 0$, h_Z [Eq. (2)] presents an opportunity to break in-plane IS turning on a finite Berry curvature distribution. For clarity, we will first focus on the case when λ and $\alpha_{x,y}$ are nonzero, while setting the k-independent terms $\delta_{x,z} = 0$, and then analyze the case when $\delta_{x,z} \neq 0$ later in the text.

To proceed, we first note that for pristine $1T'$-WTe$_2$ (when $E_\perp = 0$), the Hamiltonian $h^{\text{eff}} = h_0(\mathbf{k})$ in Eq. (1) possesses spin degenerate states $\Psi_{\tau\xi}$, with $\xi = \pm 1$ corresponding to $\uparrow$, $\downarrow$ states, and spin-degenerate energy $\varepsilon_{\tau\xi}(\mathbf{k}) = \bar{\epsilon}_{\mathbf{k}} + \tau \Delta_{\mathbf{k}}$, where $\Delta_{\mathbf{k}}^2 = (v_x k_x)^2 + (v_y k_y)^2 + m_{\mathbf{k}}^2$ is the energy difference between the conduction and valence bands. In the absence of $v_{x,y}$, conduction ($\psi_{\tau=+1,\xi}$) and valence ($\psi_{\tau=-1,\xi}$) bands touch and exhibit a gapless spectrum along Γ-Y [20]. However, large spin-selective atomic orbital coupling $v_{x,y}$ in $1T'$-WTe$_2$ creates strong interorbital mixing (between $\psi_{c,v}$) giving a large QSH gap ~ 0.055 eV [2].

Even though the external $E_\perp$ induced spin-orbit coupling [Eq. (2)] is small as compared with the intrinsic spin-selective atomic orbital coupling, $\alpha_\pm, \lambda \ll v_\pm$, nevertheless when an external electric field $E_\perp \neq 0$ is applied, IS is immediately broken. Specifically, we emphasize that it is *in-plane* IS breaking that enables a finite Berry curvature $\Omega_{\tau\xi}(\mathbf{k})$ distribution to develop. As a result, we find that λ encoding in-plane IS breaking [arising from d_x, Fig. 1(c)] turns on $\Omega_{\tau\xi}(\mathbf{k})$. In contrast, while $\alpha_{x,y}$ is also induced by $E_\perp \neq 0$ (and can also spin-split $\psi_{c,v}$ bands), it corresponds to an out-of-plane IS breaking, and does not lead to $\Omega_{\tau\xi}(\mathbf{k})$.

To see this explicitly, we first consider the case $\alpha \ll \lambda$ where out-of-plane IS breaking is much weaker than in-plane IS breaking. In this case, λ dominates $h_1(\mathbf{k})$ and we can take $\alpha \to 0$. Therefore, $h^{\text{eff}}(\mathbf{k}) = h_0(\mathbf{k}) + h_1(\mathbf{k})$ produces a $\Psi_{\tau\xi}$ band structure with a lifted spin-degeneracy [Fig. 1(e)] and energies $\varepsilon_{\tau\xi}(\mathbf{k}) = \bar{\epsilon}_{\mathbf{k}} + \tau \Delta_{\mathbf{k}} + \xi |\lambda k_y|$. We note that since both λ as well as spin-selective atomic orbital coupling $v_{x,y}$ do not mix spins, $\Psi_{\tau\xi}$ possesses spins that purely point out-of-plane [Fig. 2(b)]. Using this, we find a Berry curvature distribution $\Omega_{\tau\xi}(\mathbf{k}) = \nabla_{\mathbf{k}} \times \langle \Psi_{\tau\xi}(\mathbf{k}) | i \nabla_{\mathbf{k}} | \Psi_{\tau\xi}(\mathbf{k}) \rangle$ as

$$\Omega_{\tau\xi}^{(0)}(\mathbf{k}) = \text{sgn}(k_y) \frac{\tau\xi}{2} \frac{v_x v_y}{\Delta_{\mathbf{k}}^3} (1 - \mathbf{k} \cdot \nabla_{\mathbf{k}}) m_{\mathbf{k}}. \quad (3)$$

Strikingly, $\Omega_{\tau\xi}^{(0)}(\mathbf{k})$ in Eq. (3) does not depend on λ even though finite λ was required to break in-plane IS. Instead, $\Omega_{\tau\xi}^{(0)}(\mathbf{k})$ is solely determined by the spin-selective atomic orbital coupling $v_{x,y}$ and the band parameters in pristine $1T'$-WTe$_2$.

This decoupling behavior between IS breaking strength and the value of $\Omega_{\tau\xi}$ persists even in the presence of finite out-of-plane IS breaking characterized by the ratios λ/α. To see this, we note that when α is finite, $h_1(\mathbf{k})$ starts to hybridize
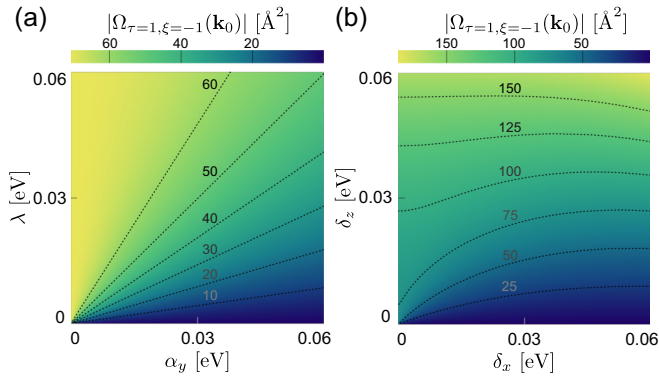
FIG. 3. Peak Berry curvature $\Omega_{\tau=1,\xi=-1}(\mathbf{k}_0)$ as a function of (a) k-dependent spin-orbit couplings (α, λ) with $\delta_{x,z} = 0$, and (b) k-independent spin-orbit couplings (δ_x, δ_z) with $\alpha, \lambda = 0$. Peaks are taken at the band edge $\mathbf{k}_0 = (0, k_0)$ with $k_0 = 0.385 \text{ Å}^{-1}$. Dashed lines denote equi-Berry-curvature contours. Both (a) and (b) show that Berry curvature is pronounced only when λ or δ_z is large; this corresponds to strong in-plane inversion symmetry breaking. Parameters for the pristine part are listed in Table III [11].

$\Psi_{\tau\xi}$ with different spins (in the same τ band). Since the intrinsic Berry curvatures $\Omega^{(0)}_{\tau\xi}(\mathbf{k})$ for spin-up and spin-down states are opposite in sign, when the ξ states couple (via α) the Berry curvature drops. Along the high-symmetry line $k_x = 0$ about which the Berry curvature is even due to the TRS and mirror symmetry in the y direction, the Berry curvature for the spin-split bands near the band edge can be expressed as [11]

$$\Omega_{\tau\xi}(k_x = 0, k_y) = \frac{\lambda}{(\lambda^2 + \alpha_y^2)^{1/2}} \Omega^{(0)}_{\tau\xi}(k_x = 0, k_y), \quad (4)$$

clearly displaying how $\Omega_{\tau\xi}(k_x = 0, k_y)$ tends to the value expected in $\Omega^{(0)}_{\tau\xi}$ for $\lambda \gg \alpha$. In Fig. 3(a), we plot the peak value of Berry curvature $\Omega_{\tau=1,\xi=-1}$ reproduced in a numerical evaluation of the SBD description. This verifies our analysis above that the value of $\Omega_{\tau\xi}$ is bounded by the intrinsic (depends only on $v_{x,y}$) $\Omega^{(0)}_{\tau\xi}$, and is tuned only by the ratios λ/α, which causes equi-Berry-curvature contours to be straight lines [see Fig. 3(a)].

We now consider the case of $\delta_{x,z} \neq 0$ while setting k-dependent terms $\alpha, \lambda = 0$. By numerically evaluating the peak Berry curvature $\Omega_{\tau=1,\xi=-1}(\mathbf{k}_0)$ [see Fig. 3(b)], we find that the peak Berry curvature $\Omega_{\tau=1,\xi=-1}(\mathbf{k}_0)$ develops a more complicated behavior. In particular, $\Omega_{\tau=1,\xi=-1}(\mathbf{k}_0)$ is no longer bounded by the intrinsic value $\Omega^{(0)}_{\tau\xi}$, and it increases with δ_z without saturation. However, similar to the previous case, out-of-plane IS breaking δ_x alone is not able to induce a nonzero Berry curvature since it corresponds to an out-of-plane IS breaking. Large Berry curvature only appears when δ_z is significant.

In the above, we concentrated on unveiling the (Berry curvature) features that the various symmetry-allowed spin-orbit coupling terms possess. These features can in turn help to diagnose which of the (a priori symmetry-allowed) spin-orbit coupling terms dominate. We illustrate this by comparing with recent first-principles calculations as well as a recent experiment [14]. In Ref. [14], the Berry curvature of monolayer $1T'$-WTe$_2$ was investigated at different perpendicular electric fields, from 0 to around 1 V nm^{-1}

using both first principles and a photocurrent measurement. In particular, their first-principles results revealed the $E_\perp$-induced spin-splitting in the band structure that vanished at larger k_y away from the band edge, and a peak Berry curvature that increased with $E_\perp$. This observation means that k-dependent spin-orbit couplings may play only a minimal role. Further, both the experiment and the first-principles calculations found large Berry curvature at the band edge, even at a small electric field, indicating that $\delta_z > \delta_x$ (see Fig. 3). Strikingly, these values of Berry curvature are close to the large intrinsic values expected from $v_{x,y}$ and $m_\mathbf{k}$. Together with Fig. 3(b), this indicates that the in-plane IS breaking and h_Z terms dominate, overwhelming the h_R terms. As a result, in what follows we will use the k-independent δ_z spin-orbit coupling term to describe the $E_\perp$-induced spin texture.

V. CURRENT-INDUCED MAGNETIZATION

Another closely related quantity, the (intrinsic) orbital magnetic moment $m^{\text{int}}_n(\mathbf{k})$, also appears when in-plane IS is broken by $E_\perp \hat{\mathbf{z}}$:

$$m^{\text{int}}_n(\mathbf{k}) = \frac{e}{\hbar} \text{Re} \sum_{n' \neq n} \frac{i \langle n|\partial H/\partial k_x|n'\rangle \langle n'|\partial H/\partial k_y|n\rangle}{\varepsilon_n - \varepsilon_{n'}}, \quad (5)$$

where we have written $n = \{\tau\xi\}$ as a short-hand, and H is the Hamiltonian. The orbital magnetic moment comes from the self-rotation of a Bloch electron wave packet around its center of mass, it is an intrinsic property of the Bloch band [21], and its distribution in momentum space mimics that of the Berry curvature distribution (see the Appendix [11]).

The low-symmetry of $1T'$-WTe$_2$ enables an asymmetric distribution of $\Omega_n(\mathbf{k})$ and $m_n(\mathbf{k})$ [see Figs. 4(a) and 4(b)]. This affords the opportunity to realize Berry phase effects not normally achievable in their rotational symmetric cousins. A striking example is the (linear) magnetoelectric effect (ME) $M_z = \sum_i \alpha_{zi} E_i$ $(i = x, y)$, where the flow of an in-plane current induces an out-of-plane magnetization. While typically found in multiferroic materials [22] where TRS and IS are explicitly broken, ME effects can arise in metals with sufficiently low symmetry (broken IS as well as broken rotational symmetry), and where the dissipation of a charge current breaks TRS [23]. This is termed the kinetic ME effect [23,24].

The requirements for the kinetic ME effect can be seen from a symmetry analysis as follows: (a) in a time-reversal symmetric system $M_z = \sum_i \alpha_{zi} E_i$, then under the symmetry operation $t \to -t$ we have $M_z \to -M_z$, $\mathbf{E} \to \mathbf{E}$, and $M_z = \sum_i \alpha_{zi} E_i \to -M_z = \sum_i \alpha_{zi} E_i$, which leads to $\alpha_{zx} = \alpha_{zy} = 0$; (b) if a system has a rotational symmetry, then under the rotation by angle θ we have $M_z \to M_z$, $E_x \to E_x \cos\theta - E_y \sin\theta$, $E_y \to E \sin\theta + E_y \cos\theta$, and $M_z = \alpha_{zx} E_x + \alpha_{zy} E_y \to M_z = (\alpha_{zx} E_x + \alpha_{zy} E_y) \cos\theta + (\alpha_{zy} E_x - \alpha_{zx} E_y) \sin\theta$, which leads to $\theta = 2n\pi$ $(n = 0, 1, 2, \ldots)$, i.e., rotational symmetry is not allowed for nonzero α_{zx} and α_{zy}; (c) if a system is centrosymmetric, then under the operation $(x, y) \to (-x, -y)$ we have $M_z \to M_z$, $\mathbf{E} \to -\mathbf{E}$, and $M_z = \sum_i \alpha_{zi} E_i \to M_z = -\sum_i \alpha_{zi} E_i$, which also requires $\alpha_{zx} = \alpha_{zy} = 0$.

Indeed, the low symmetry of $1T'$-WTe$_2$ (with $E_\perp \neq 0$) where only a mirror symmetry in the y direction remains is
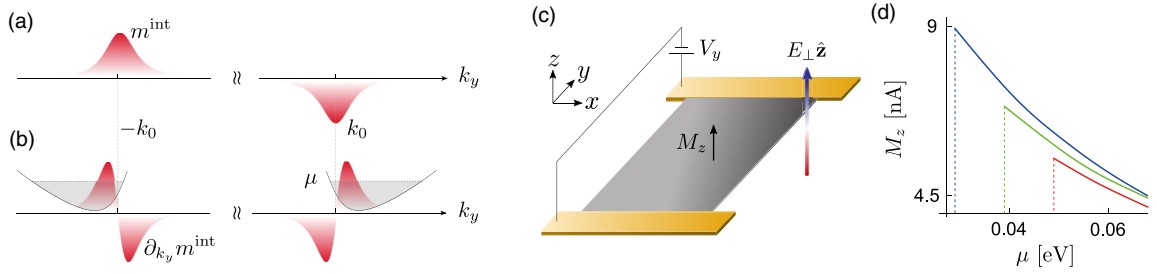
FIG. 4. (a,b) Asymmetry in $1T'$-WTe$_2$ enables dipolar distributions of the intrinsic magnetic moment (a) m^{int} characterized by (b) $\partial_{k_y} m^{\text{int}}$ near the gap openings $\pm \mathbf{k}_0 = (0, \pm k_0)$. Black curves represent the conduction band ($\tau = 1, \xi = -1$) and dashed lines denote the chemical potential μ, with gray-shaded areas the occupied states. Due to the tilt of the band dispersion, an intrinsic magnetic moment dipole arises near the gap opening and gives rise to a nonzero current-induced magnetization M_z [see Eq. (6)]. Parameters used for the pristine part are the same as those in Fig. 1 as an illustration. (c) Schematic of a $1T'$-WTe$_2$ monolayer under a perpendicular electric field $E_\perp \hat{\mathbf{z}}$ and an in-plane electric field E_y, which can give rise to intrinsic magnetization M_z. (d) Calculated intrinsic magnetization M_z induced by a current $j_y = 10 \text{ A m}^{-1}$ in the y direction from Eq. (6), with $\lambda, \alpha, \delta_x = 0$, but varying $\delta_z = 0.075$ eV (blue), 0.05 eV (green), and 0.025 eV (red). These magnitudes for δ_z are within reach by applying $E_\perp < 1 \text{ V nm}^{-1}$ [14]. The M_z plotted here becomes nonzero only when the chemical potential is above the conduction-band bottom (denoted by dashed lines), which is different for each of the lines. The trend from the red line to the blue line shows that a larger δ_z (stronger in-plane IS breaking) leads to an increased intrinsic magnetic moment as well as more pronounced M_z, as illustrated in Fig. 2.

the largest symmetry group that hosts the kinetic ME [7,23]. This makes $1T'$-WTe$_2$ a natural venue to control ME.

To illustrate the kinetic ME effect in $1T'$-WTe$_2$, we first note that the magnetic moment is asymmetric, displaying a dipolar distribution [see Figs. 4(a) and 4(b)]. This can be seen explicitly by considering $\partial_{k_y} m$ and noting that it is displaced in relation to the bottom of the band, Fig. 4(b). As a result, when an in-plane electric field shifts the distribution function, a uniform out-of-plane magnetization M_z develops:

$$M_z = \sum_{i=x,y} \tilde{\alpha}_{zi} j_i, \quad \tilde{\alpha}_{zi} = \left[\frac{e}{\hbar} \sum_{n,\mathbf{k}} f_{n\mathbf{k}}^{(0)} \frac{\partial m_n^{\text{tot}}(\mathbf{k})}{\partial k_i} \right] (D_{ii})^{-1},$$

(6)

where D_{ii} is the Drude weight along the i direction, $f_{n\mathbf{k}}^{(0)}$ is the equilibrium distribution function, and $m_n^{\text{tot}}(\mathbf{k}) = m_n^{\text{int}}(\mathbf{k}) + (ge/2m_0)\langle u_\mathbf{k}|s_z|u_\mathbf{k}\rangle$ is the intrinsic contribution to the magnetic moment in a particular band, containing both orbital and spin contributions with $s_z = \hbar\sigma_z/2$. For $1T'$-WTe$_2$ monolayer, we estimate $g \sim 5$ [3,4].

Importantly, Eq. (6) reflects the symmetry of the crystal. For example, magnetic moment distribution has equal magnitudes but opposite signs in the two electron pockets in the conduction band. As a result, $\tilde{\alpha}_{zx} = 0$ vanishes as expected from symmetry; see above. In contrast, when an in-plane electric field is applied along y, a nonzero M_z is generated (i.e., $\tilde{\alpha}_{zy} \neq 0$).

Using Eq. (6), we obtain a finite out-of-plane magnetization M_z in Fig. 4(d) when current is driven along the y direction. In doing so, we used $f_{n\mathbf{k}}^{(0)} = \Theta(\varepsilon_{n\mathbf{k}} - \mu)$ with μ the chemical potential, and we computed the Drude weight in the usual fashion. Further, to capture the full reciprocal space distribution of the magnetic moment (including regions away from the gap opening), we used the SBD description to compute the magnetic moment distribution. Here we have concentrated on small chemical potentials so that only moments in the lowest conduction band [the blue band in Fig. 1(e)] contribute. Since $m_n^{\text{int}}(\mathbf{k})$ is an odd function of k_y

when TRS is present, the filled bands do not contribute to ME. This reflects the fact that kinetic ME arises from a dissipative process. As a result, when the chemical potential is in the gap, $\tilde{\alpha}_{zy} = 0$. However, once the system is doped into the conduction band, a nonzero ME develops; see Fig. 4(d). A similar analysis also applies to the Berry curvature $\Omega_{\tau\xi}$ (which exhibits a dipolar distribution), and leads to a nonlinear Hall effect without an applied magnetic field (see Ref. [7] as well as the Appendix [11] for an explicit discussion of this system).

VI. SUMMARY

$1T'$-WTe$_2$ with an applied out-of-plane electric field $E_\perp$ provides a new and compelling venue to control bulk band quantum geometry. In particular, its bands exhibit a tunable Berry curvature and magnetic moment with switchlike behavior. Crucially, the low symmetry of its crystal structure enables effects not normally found in its rotationally symmetric cousins. These include striking Berry phase effects such as a current-induced magnetization (ME) and a quantum nonlinear Hall effect. These are particularly sensitive to the orientation of an in-plane electric field and the crystallographic directions. Indeed, M_z is strongest when current runs along the y direction; this sensitivity can be verified through measurements in a single $1T'$-WTe$_2$ sample for, e.g., using a Corbino disk geometry. Perhaps most exciting, however, is how IS broken $1T'$-WTe$_2$ enables direct and electric-field tunable access to out-of-plane magnetic degrees of freedom. Given its two-dimensional nature, $1T'$-WTe$_2$ can be stacked with other two-dimensional materials, providing a key magnetoelectric component in creating magnetic van der Waals heterostructures.

APPENDIX

1. Six-band $\mathbf{k} \cdot \mathbf{p}$ model for monolayer $1T'$-WTe$_2$

Without external fields, $1T'$-WTe$_2$ monolayers possess time-reversal (TR) symmetry and a point symmetry group $P2_1/m$ that contains four symmetry operations. If we set one of the inversion centers as the origin $O_0 = (0, 0, 0)$ in real space, the four symmetry operations are $\{(x, y, z), (-x, -y, -z), (x, 1/2 - y, z), (-x, 1/2 + y, -z)\}$, where $1/2$ denotes a shifting $1/2$ unit cell in the y direction. When we shift the origin O_0 to $O_1 = (0, 1/2, 0)$, the four symmetry operations become $\{(x, y, z), (x, -y, z), (-x, 1/2, -z), (-x, -1/2, -z)\}$.

Various first-principles calculations as well as experimental measurements [1,2,12,13] showed that there are three relevant orbitals contributing to the states near the gap. Although the exact orbital compositions at the Γ point are not clear, these orbitals at the Γ point are consistently revealed [2,12,13] to be (even, odd, even) under the reflection operation in the y direction (the orbitals are ordered with decreasing energy). Here we note that Choe *et al.* used a different coordinate system with x and y directions exchanged.

A perpendicularly applied electric field breaks symmetry operations that flip in the z direction and reduce the point group $P2_1/m$ to group C_{1v} that has only two symmetry operations $\{\mathbb{I}, M_y\}$ (i.e., identity and reflection about the xz plane that cross a Te atom). It has two real 1D irreducible representations (see Table I).

Aside from the spin degrees of freedom, each of the three orbitals at the Γ point is nondegenerate and transforms according to one of the 1D irreducible representations of C_{1v}. Moreover, although inversion symmetry is broken, the three orbitals remain (even, odd, even) in the y direction at the Γ point. These two observations show that the three orbitals at the Γ point transform as

$$\psi_1 \sim 1, \quad \psi_2 \sim y, \quad \psi_3 \sim 1, \tag{A1}$$

where the symbol "$\sim$" denotes how these functions transform under operations in C_{1v}. Using $\{\psi_1, \psi_2, \psi_3\}$ as a basis, the $\mathbf{k} \cdot \mathbf{p}$ Hamiltonian near the Γ point assumes a 3×3 form:

$$H(\mathcal{K}) = \begin{pmatrix} H^{11}(\mathcal{K}) & H^{12}(\mathcal{K}) & H^{13}(\mathcal{K}) \\ H^{21}(\mathcal{K}) & H^{22}(\mathcal{K}) & H^{23}(\mathcal{K}) \\ H^{31}(\mathcal{K}) & H^{32}(\mathcal{K}) & H^{33}(\mathcal{K}) \end{pmatrix}, \tag{A2}$$

where $H^{\alpha\beta}(\mathcal{K})$ is the 2×2 (1×1) block matrix between ψ_1 and ψ_2 with (without) a spin degree of freedom included.

In the following, we will obtain the general form of $H(\mathcal{K})$ from symmetry analysis. The necessary information for $\psi_{1,2,3}$ is contained in its transformation property under group C_{1v} [Eq. (A1)]. We note that detailed orbital compositions, e.g., the weight of a p or d orbital in $|\psi_{1,2,3}\rangle$, does not affect the following analysis.

We will proceed by using the theory of invariants [16,25,26], which is based on the invariance of the Hamiltonian $\hat{H}$ under all operations of the corresponding crystal symmetry group. When the Hamiltonian $\hat{H}$

TABLE I. The character table for the group C_{1v}, and corresponding operator combinations that are even (first row) and odd (second row) under M_y. s_0 is the 2×2 identity matrix. Note that the prefactor i in some of the terms guarantees TR symmetry, since i, $\mathbf{k}$, and $\mathbf{s}$ are odd under the TR operation. Here we only keep terms up to $O(k^2)$ in the diagonal part and $O(k)$ in the off-diagonal part.

C_{1v}	$\mathbb{I}$	M_y	TR invariant operators
Γ_1	1	1	s_0, ik_x, k_x^2, k_y^2, is_y, $k_x s_y$, $k_y s_x$, $k_y s_z$
Γ_2	1	-1	ik_y, is_x, is_z, $k_x s_x$, $k_x s_z$, $k_y s_y$

is projected to the energy bands of interest, $\hat{H} = \sum_{\alpha,\beta} |\psi_\alpha\rangle H^{\alpha\beta}(\mathcal{K}) \langle\psi_\beta|$, where $\mathcal{K}$ denotes a tensor operator formed by combinations of wave vectors, the symmetry group constrains the $\mathbf{k} \cdot \mathbf{p}$ Hamiltonian $H^{\alpha\beta}(\mathcal{K})$ as follows: under an arbitrary symmetry operation $g \in C_{1v}$, the basis $|\psi_\alpha\rangle$ transforms according to the irreducible representation Γ_α, so the invariance of the Hamiltonian under the symmetry operation g dictates $\hat{P}_g \hat{H} \hat{P}_g^{-1} = \hat{H}$, where $\hat{P}_g$ denotes the operator for symmetry operation g. This leads to $\sum_{\alpha',\beta'} \langle\psi_\alpha|\hat{P}_g|\psi_{\alpha'}\rangle H^{\alpha'\beta'}(\hat{P}_g \mathcal{K} \hat{P}_g^{-1}) \langle\psi_{\beta'}|\hat{P}_g^{-1}|\psi_\beta\rangle = H^{\alpha\beta}(\mathcal{K})$, or equivalently,

$$\mathbf{D}^\alpha(g) H^{\alpha\beta}(\hat{P}_g \mathcal{K} \hat{P}_g^{-1}) \mathbf{D}^\beta(g^{-1}) = H^{\alpha\beta}(\mathcal{K}), \tag{A3}$$

where $\langle\psi_\alpha|\hat{P}_g|\psi_{\alpha'}\rangle = \delta_{\alpha\alpha'}\mathbf{D}^\alpha(g)$, with $\mathbf{D}^\alpha(g)$ the representation matrix of g in Γ_α (in the 1D irreducible representation case here, 1 or -1), and $\hat{P}_g \mathcal{K} \hat{P}_g^{-1}$ denotes the transformation of $\mathcal{K}$ under the symmetry operation g, e.g., if $g = M_y$ and $\mathcal{K} = k_y$, then $\hat{P}_{M_y} k_y \hat{P}_{M_y}^{-1} = -k_y$.

In constructing the $\mathcal{K}$ operators, one can also take into account the spin degree of freedom by including the spin operator $\mathbf{s} = (s_x, s_y, s_z)$ in the $\mathbf{k} \cdot \mathbf{p}$ Hamiltonian. Note that $\mathbf{s}$ is a pseudovector. We have $s_x \to -s_x$, $s_z \to -s_z$, and $s_y \to s_y$ under the operation M_y [26], e.g., if $g = M_y$ and $\mathcal{K} = k_y s_x$, then $\hat{P}_{M_y} k_y s_x \hat{P}_{M_y}^{-1} = (\hat{P}_{M_y} k_y \hat{P}_{M_y}^{-1})(\hat{P}_{M_y} s_x \hat{P}_{M_y}^{-1}) = (-k_y)(-s_x) = k_y s_x$.

For general cases in which crystals have high-symmetry point groups, the expression of an arbitrary block $H^{\alpha\beta}(\mathcal{K})$ of the $\mathbf{k} \cdot \mathbf{p}$ Hamiltonian can be constructed in several standard procedures with the corresponding full character table [16,25,26]. In our case, however, the group C_{1v} is the simplest nontrivial group that has only two symmetry operations $\{\mathbb{I}, M_y\}$, and we can do the analysis just based on mirror symmetry operation M_y:

(i) For blocks $H^{\alpha\alpha}(\mathcal{K})$ ($\alpha = 1, 2, 3$) and $H^{13}(\mathcal{K})$: since $|\psi_\alpha\rangle\langle\psi_\alpha|$ ($\alpha = 1, 2, 3$) and $|\psi_1\rangle\langle\psi_3|$ are even under M_y operation, to make sure $\hat{H}$ is invariant under M_y operation, then $H^{\alpha\alpha}(\mathcal{K})$ ($\alpha = 1, 2, 3$) and $H^{13}(\mathcal{K})$ must be composed by $\mathcal{K}$ operators that are also even under M_y operation. Relevant operator combinations that are invariant under M_y operation are listed in the first row of Table I.

(ii) For blocks $H^{12}(\mathcal{K})$ and $H^{23}(\mathcal{K})$: since $|\psi_1\rangle\langle\psi_2|$ and $|\psi_2\rangle\langle\psi_3|$ are odd under M_y operation, then $H^{12}(\mathcal{K})$ and $H^{23}(\mathcal{K})$ must be composed by $\mathcal{K}$ operators that are also odd under M_y operation to ensure that $\hat{H}$ is invariant under M_y operation. Relevant operator combinations that are odd under M_y are listed in the second row of Table I.

TABLE II. Terms that can appear for $\mathbf{k} \cdot \mathbf{p}$ Hamiltonian blocks. The prefactor i in some of the terms guarantees TR symmetry, since i, $\mathbf{k}$, and $\mathbf{s}$ are odd under the TR operation. s_0 is the 2×2 identity matrix. As in Table I, we kept terms up to $O(k^2)$ in the diagonal part and $O(k)$ in the off-diagonal part.

	$H^{\alpha\alpha}(\mathcal{K})$	$H^{12}(\mathcal{K}),\ H^{23}(\mathcal{K})$
with or w/o $E\hat{z}$	$s_0,\ k_x^2 s_0,\ k_y^2 s_0$	$ik_y s_0,\ k_x s_z$
with $E\hat{z}$	$k_y s_z;\ k_x s_y,\ k_y s_x$	$is_z;\ is_x$

After obtaining the terms that transform correctly for each of the blocks, we note further constraints that trim the $\mathbf{k} \cdot \mathbf{p}$ Hamiltonian:

(1) The $\mathbf{k} \cdot \mathbf{p}$ Hamiltonian must be Hermitian, which dictates that the invariants for a diagonal block must be Hermitian.

(2) Terms containing both $\mathbf{k}$ and $\mathbf{s}$ are matrix elements of the microscopic spin-orbit interaction $\hat{H}_{\rm so}(\mathbf{k}) \sim \mathbf{k} \cdot [\mathbf{s} \times \nabla V(\mathbf{r})]$ in $\hat{H}$, thus terms $k_x s_x$ and $k_y s_y$ will not appear.

(3) For our purposes of estimating the Berry curvature and orbital magnetic moments in the main text, we can neglect the H^{13} block. This is because $|\psi_1\rangle$ and $|\psi_3\rangle$ are energetically far away from each other ($\gtrsim 0.5$ eV) and their couplings only have small contributions to Berry curvature and orbital magnetic moment for the conduction bands. Although H^{13} block contributes to optical transitions $\gtrsim 0.5$ eV, this is beyond our current scope.

The above three considerations trim/eliminate the terms $\{ik_x, is_y, k_x s_x, k_y s_y\}$. For the remaining terms, we group them into terms induced by the applied perpendicular electric field, and those that are present in pristine $1T'$-WTe$_2$. To do so, we perform the following symmetry analysis: when the electric field is not present, inversion symmetry about the inversion center O_0 is recovered, and the operation $(-x, 1/2, -z)$ about O_1 becomes a symmetry operation again. Under the operation $(-x, 1/2, -z)$, there is no flip in the y direction while $(k_x, k_y) \rightarrow (-k_x, k_y)$ and $(s_x, s_y, s_z) \rightarrow (-s_x, s_y, -s_z)$. We can see that terms $\{is_x, is_z, k_x s_y, k_y s_x, k_y s_z\}$ change sign under this new operation, i.e., they are not invariant under the original symmetry group $P2_1/m$ and can appear only when the perpendicular electric field is applied.

After trimming, classification, and analyzing the physical origin of the terms induced by electric field, we now obtain the general form of the $\mathbf{k} \cdot \mathbf{p}$ Hamiltonian (see Table II).
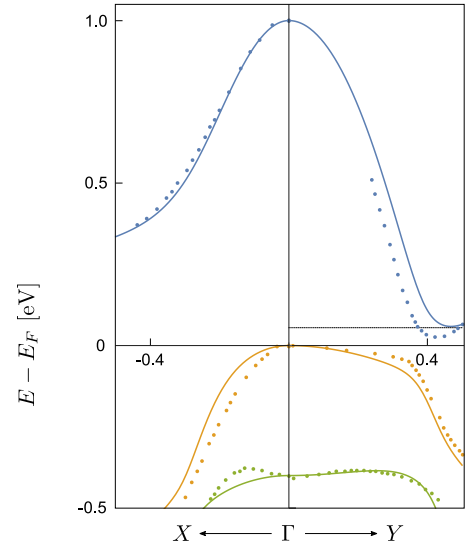

FIG. 5. Energy dispersion near the Fermi surface from the model Eq. (A4), with an overall band gap 0.055 eV [2], indicated by the dashed line) (solid lines). Data (dots) extracted from Refs. [1,14]. The parameters for the model are listed in Table III.

First we use a least-squares fitting to extract coefficients of these invariant operators from known band structure, either from experimental measurements or numerical calculations. From the first-principles calculation result [1,14], we obtained the Hamiltonian $H_0(\mathbf{k})$ when there is no external field. We find

$$H_0(\mathbf{k}) = \begin{pmatrix} \epsilon_1 & 0 & v_1^+ & 0 & 0 & 0 \\ 0 & \epsilon_1 & 0 & v_1^- & 0 & 0 \\ -v_1^- & 0 & \epsilon_2 & 0 & v_3^+ & 0 \\ 0 & -v_1^+ & 0 & \epsilon_2 & 0 & v_3^- \\ 0 & 0 & -v_3^- & 0 & \epsilon_3 & 0 \\ 0 & 0 & 0 & -v_3^+ & 0 & \epsilon_3 \end{pmatrix}, \quad (A4)$$

where $\epsilon_i = c_{i,0} + c_{i,x}k_x^2 + c_{i,y}k_y^2$ and $v_i^\pm = \pm v_{i,x}k_x + i v_{i,y}k_y$. The dispersion is plotted in Fig. 5, with parameters listed in Table III.

The additional terms that are induced by the applied perpendicular electric field $E_\perp$ make the full Hamiltonian $H(\mathbf{k}) = H_0(\mathbf{k}) + H_1(\mathbf{k})$, with

$$H_1(\mathbf{k}) = \begin{pmatrix} \lambda_1 k_y & \alpha_1^- & i\delta_{1,z} & i\delta_{1,x} & 0 & 0 \\ \alpha_1^+ & -\lambda_1 k_y & i\delta_{1,x} & -i\delta_{1,z} & 0 & 0 \\ -i\delta_{1,z} & -i\delta_{1,x} & \lambda_2 k_y & \alpha_2^- & i\delta_{3,z} & i\delta_{3,x} \\ -i\delta_{1,x} & i\delta_{1,z} & \alpha_2^+ & -\lambda_2 k_y & i\delta_{3,x} & -i\delta_{3,z} \\ 0 & 0 & -i\delta_{3,z} & -i\delta_{3,x} & \lambda_3 k_y & \alpha_3^- \\ 0 & 0 & -i\delta_{3,x} & i\delta_{3,z} & \alpha_3^+ & -\lambda_3 k_y \end{pmatrix}, \quad (A5)$$

where $\alpha_i^\pm = \pm i\alpha_{i,x}k_x + \alpha_{i,y}k_y$ is the commonly seen spin-orbit coupling for the ith orbital (this is sometimes referred to as "Rashba" spin texture), $\lambda_i k_y$ is a spin splitting from in-plane IS breaking, and $\delta_{i,x}$ and $\delta_{i,z}$ are k-independent interband couplings; see the main text for a discussion of the physical origin.

TABLE III. Least-squares fitted $\mathbf{k} \cdot \mathbf{p}$ parameters for a $1T'$-WTe$_2$ monolayer without external fields from Refs. [1,14], with an overall band gap 0.055 eV.

Parameter	Value	Unit	Parameter	Value	Unit
$c_{1,0}$	1.0	eV			
$c_{2,0}$	0	eV			
$c_{3,0}$	-0.4	eV			
$c_{1,x}$	-11.25	eV Å^2	$c_{1,y}$	-6.90	eV Å^2
$c_{2,x}$	-0.27	eV Å^2	$c_{2,y}$	-1.08	eV Å^2
$c_{3,x}$	-0.82	eV Å^2	$c_{3,y}$	0.99	eV Å^2
$v_{1,x}$	1.71	eV Å	$v_{1,y}$	0.48	eV Å
$v_{3,x}$	0.48	eV Å	$v_{3,y}$	-0.48	eV Å

2. 4 × 4 model near the band gap

To obtain the effective 4×4 Hamiltonian near the band gap, we consider the energy eigenvalue equation

$$\begin{pmatrix} h_q & u \\ u^\dagger & h_d \end{pmatrix} \begin{pmatrix} \psi_q \\ \psi_d \end{pmatrix} = \varepsilon \begin{pmatrix} \psi_q \\ \psi_d \end{pmatrix}, \tag{A6}$$

where h_q (h_d) is the 4×4 (2×2) diagonal block from the original 6×6 Hamiltonian, ψ_q (ψ_d) is the corresponding four (two) -component state vector, and u is the 4×2 matrix couple h_q and h_d.

The second row of Eq. (A6) allows ψ_d to be written in terms of ψ_q:

$$\psi_d = (\varepsilon - h_d)^{-1} u^\dagger \psi_q. \tag{A7}$$

Substituting this into the first row of Eq. (A6) gives an effective eigenequation solely for the ψ_q components:

$$\left[h_q + u(\varepsilon - h_d)^{-1} u^\dagger \right] \psi_q = \varepsilon \psi_q. \tag{A8}$$

Performing the standard expansion in small ε as well as the rotation procedure [25], we obtain the effective Hamiltonian near the band gap as

$$\tilde{h}_q = \mathcal{S}^{-1/2} \left(h_q - u h_d^{-1} u^\dagger \right) \mathcal{S}^{-1/2}, \quad \mathcal{S} = 1 + u h_d^{-2} u^\dagger, \tag{A9}$$

valid when ε is small, and we have used the rotated basis $\psi = \mathcal{S}^{1/2} \psi_q$.

Following the above analysis, we now derive the 4×4 model for the pristine part. From Eq. (A4) we have

$$h_q = \begin{pmatrix} \epsilon_1 & 0 & v_1^+ & 0 \\ 0 & \epsilon_1 & 0 & v_1^- \\ -v_1^- & 0 & \epsilon_2 & 0 \\ 0 & -v_1^+ & 0 & \epsilon_2 \end{pmatrix}, \tag{A10}$$

$$u^\dagger = \begin{pmatrix} 0 & 0 & v_3^+ & 0 \\ 0 & 0 & 0 & v_3^- \end{pmatrix}, \tag{A11}$$

and

$$h_d = \begin{pmatrix} \epsilon_3 & 0 \\ 0 & \epsilon_3 \end{pmatrix}, \tag{A12}$$

where $\epsilon_i = c_{i,0} + c_{i,x} k_x^2 + c_{i,y} k_y^2$ and $v_i^\pm = \pm v_{i,x} k_x + i v_{i,y} k_y$. Using h_d and u above, we have

$$\tilde{h}_q = \begin{pmatrix} \epsilon_c & 0 & v^+ & 0 \\ 0 & \epsilon_c & 0 & v^- \\ -v^- & 0 & \epsilon_v & 0 \\ 0 & -v^+ & 0 & \epsilon_v \end{pmatrix}, \tag{A13}$$

where $\epsilon_c = \epsilon_1$, and

$$\epsilon_v = \frac{1}{1+r} \epsilon_2 - \frac{r}{1+r} \epsilon_3, \quad v = \sqrt{\frac{1}{1+r}} v_1. \tag{A14}$$

Here the k-dependent ratio r is

$$r = \frac{(v_{3,x} k_x)^2 + (v_{3,y} k_y)^2}{\epsilon_3^2}, \tag{A15}$$

which controls the renormalization of ϵ_2 and v_1. It becomes zero when $v_3 = 0$, i.e., when ψ_2 and ψ_3 do not couple with each other, $r = 0$, and there is no renormalization. We note that the form of this pristine part in Eq. (A13) is consistent with the model proposed in Ref. [1]; for a full discussion, see Appendix Sec. 6.

If we reorder the basis to $\{\psi_{c\uparrow}, \psi_{v\uparrow}; \psi_{c\downarrow}, \psi_{v\downarrow}\}$, this gives the BHZ-type pristine part,

$$h_0 = \bar{\epsilon} + \begin{pmatrix} m & v^+ & 0 & 0 \\ -v^- & -m & 0 & 0 \\ 0 & 0 & m & v^- \\ 0 & 0 & -v^+ & -m \end{pmatrix}, \tag{A16}$$

where $\bar{\epsilon} = (\epsilon_c + \epsilon_v)/2$, $m = (\epsilon_c - \epsilon_v)/2$. Together with the electric-field-induced part (neglecting the far away ψ_3 band),

$$h_1 = \begin{pmatrix} \lambda k_y & i\delta_z & \alpha^- & i\delta_x \\ -i\delta_z & \lambda k_y & i\delta_x & \alpha^- \\ \alpha^+ & -i\delta_x & -\lambda k_y & -i\delta_z \\ -i\delta_x & \alpha^+ & i\delta_z & -\lambda k_y \end{pmatrix}, \tag{A17}$$

we obtained the 4×4 effective Hamiltonian near the gap opening,

$$h^{\text{eff}} = h_0 + h_1. \tag{A18}$$

When focusing on the dispersions and Berry curvatures near the gap opening, we find a convenient estimate for v:

$$v = \sqrt{\frac{1}{1+r_0}} v_1, \quad r_0 = r(\mathbf{k}_0), \tag{A19}$$

where $\mathbf{k}_0 = (0, k_0)$ is the position of the band edge with $k_0 = 0.385$ Å^{-1}. By doing this, we obtained the dispersion and a Berry curvature distribution that agree well with the six-band model near the gap opening [see the solid and dashed lines in Figs. 1(d) and 1(e) for comparison].

3. Berry curvature at the band edge from the 4 × 4 model ($\delta_{x,z} = 0$ case)

Using the 4×4 band model [see Eqs. (1) and (2) of the main text] to describe $1T'$-WTe$_2$, we can express its Berry curvature near the band edge analytically.

Without the electric-field-induced part h_1, the BHZ-type pristine part h_0 can be viewed as two decoupled 2×2 blocks:

spin-up block $h_\uparrow$ and spin-down block $h_\downarrow$. The two blocks form a time-reversal pair

$$h_\uparrow(\mathbf{k}) = h_\downarrow^*(-\mathbf{k}) = \bar{\epsilon}_\mathbf{k} + \begin{pmatrix} m_\mathbf{k} & v_\mathbf{k}^+ \\ -v_\mathbf{k}^- & -m_\mathbf{k} \end{pmatrix}, \quad (A20)$$

where $v_\mathbf{k}^\pm = \pm v_x k_x + i v_y k_y$. The two 2×2 blocks share the same dispersion relation and are spin-degenerate:

$$\varepsilon_{\tau\uparrow\downarrow}^{(0)}(\mathbf{k}) = \bar{\epsilon}_\mathbf{k} \pm \tau \Delta_\mathbf{k}, \quad \Delta_\mathbf{k} = \sqrt{(v_x k_x)^2 + (v_y k_y)^2 + m_\mathbf{k}^2}, \quad (A21)$$

with the corresponding eigenstates:

$$\psi_{\tau\uparrow}^{(0)}(\mathbf{k}) \sim (m_\mathbf{k} + \tau \Delta_\mathbf{k}, -v_\mathbf{k}^-, 0, 0)^T,$$
$$\psi_{\tau\downarrow}^{(0)}(\mathbf{k}) \sim (0, 0, m_\mathbf{k} + \tau \Delta_\mathbf{k}, -v_\mathbf{k}^+)^T, \quad (A22)$$

where $\tau = \pm$ denotes the conduction or valence band, and $2\Delta_\mathbf{k}$ is the energy difference between the conduction and valence bands.

When an external perpendicular electric field is applied, and if the spin-orbit couplings induced by the field are much weaker than the atomic spin-orbit couplings ($\alpha_{x,y}, \lambda \ll v_{x,y}$), we then treat $h_1(\mathbf{k})$ as a small perturbation to the pristine part $h_0(\mathbf{k})$. We first note that for nonzero α, and within the framework of degenerate perturbation (i.e., neglecting states that are far away in energy), $h_1(\mathbf{k})$ hybridizes the unperturbed spin-up state $\psi_{\tau\uparrow}^{(0)}(\mathbf{k})$ and spin-down state $\psi_{\tau\downarrow}^{(0)}(\mathbf{k})$ in the same band τ into spin-split states $\psi_{\tau\xi}(\mathbf{k})$, with higher ($\xi = +1$) or lower ($\xi = -1$) energies:

$$\psi_{\tau\xi}(\mathbf{k}) = c_{\tau\uparrow}^\xi(\mathbf{k}) \psi_{\tau\uparrow}^{(0)}(\mathbf{k}) + c_{\tau\downarrow}^\xi(\mathbf{k}) \psi_{\tau\downarrow}^{(0)}(\mathbf{k}). \quad (A23)$$

Interestingly, in the $\alpha \ll \lambda, \delta_z$ limit, the unperturbed spin-up state $\psi_{\tau\uparrow}^{(0)}(\mathbf{k})$ and spin-down state $\psi_{\tau\downarrow}^{(0)}(\mathbf{k})$ do not hybridize with each other. Even so, their degeneracies are lifted by λk_y:

$$\psi_{\tau\pm}(\mathbf{k}) = \psi_{\tau\uparrow\downarrow}^{(0)}(\mathbf{k}), \quad \varepsilon_{\tau\xi}(\mathbf{k}) = \bar{\epsilon}_\mathbf{k} + \tau \Delta_\mathbf{k} + \xi|\lambda k_y|. \quad (A24)$$

The Berry curvatures for these nondegenerate states $\psi_{\tau\xi}$ are well defined and read

$$\Omega_{\tau\xi}^{(0)}(\mathbf{k}) = \mathrm{sgn}(k_y) \frac{\tau\xi}{2} \frac{v_x v_y}{\Delta_\mathbf{k}^3} (1 - \mathbf{k} \cdot \nabla) m_\mathbf{k}. \quad (A25)$$

When $\alpha \sim \lambda$, the spin-up state $\psi_{\tau\uparrow}^{(0)}(\mathbf{k})$ and the spin-down state $\psi_{\tau\downarrow}^{(0)}(\mathbf{k})$ start to hybridize to form the spin-split states $\psi_{\tau\xi}$. The Berry curvature amplitudes for these hybridized states $\psi_{\tau\xi}(\mathbf{k})$ are smaller than that of $\psi_{\tau\uparrow\downarrow}^{(0)}(\mathbf{k})$ because the spin-up and spin-down states have opposite Berry curvatures.

The general form of the Berry curvature $\Omega_{\tau\xi}(\mathbf{k})$ for $\psi_{\tau\xi}(\mathbf{k})$ is complicated. Fortunately, along $k_x = 0$ about which the Berry curvature is even, i.e., $\Omega(k_x, k_y) = \Omega(-k_x, k_y)$, which comes from the TRS and the mirror symmetry in the y direction, its analytical form is greatly simplified:

$$\Omega_{\tau\xi}(0, k_y) = |c_{\tau\uparrow}^\xi|^2 \Omega_{\tau\uparrow}^{(0)}(0, k_y) + |c_{\tau\downarrow}^\xi|^2 \Omega_{\tau\downarrow}^{(0)}(0, k_y)$$
$$= (|c_{\tau\uparrow}^\xi|^2 - |c_{\tau\downarrow}^\xi|^2) \Omega_{\tau\uparrow}^{(0)}(0, k_y), \quad (A26)$$
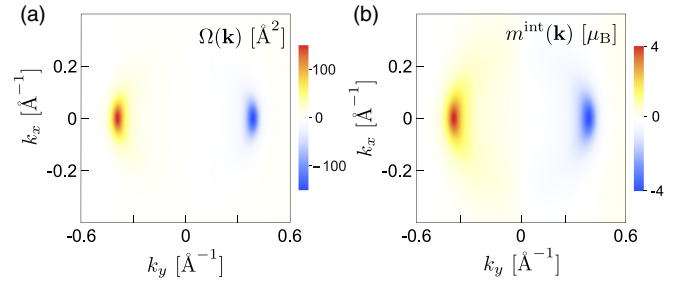

FIG. 6. (a,b) Berry curvature and magnetic moment distribution for the spin-split conduction band with lower energy in k space. Parameters for the pristine part H_0 are listed in Table III, while for H_1 we used α, λ, $\delta_x = 0$, and $\delta_z = 0.025$ eV.

where $c_{\tau\uparrow}^\xi$ and $c_{\tau\downarrow}^\xi$ satisfy

$$|c_{\tau\uparrow}^\xi|^2 - |c_{\tau\downarrow}^\xi|^2 = \tau\xi \frac{\lambda \, \mathrm{sgn}(k_y)}{(\alpha_y^2 + \lambda^2)^{1/2}}. \quad (A27)$$

With this, the Berry curvature $\Omega_{\tau\xi}(\mathbf{k})$ at the band edge $\mathbf{k}' = (k_x = 0, k_y)$ is

$$\Omega_{\tau\pm}(\mathbf{k}') = \frac{\lambda \, \mathrm{sgn}(k_y)}{(\lambda^2 + \alpha_y^2)^{1/2}} \frac{\tau\xi}{2} \frac{v_x v_y}{\Delta_{\mathbf{k}'}^3} (1 - \mathbf{k}' \cdot \nabla) m_{\mathbf{k}'}$$
$$= \frac{\lambda}{(\lambda^2 + \alpha_y^2)^{1/2}} \Omega_{\tau\uparrow\downarrow}^{(0)}(\mathbf{k}'). \quad (A28)$$

4. Berry curvature and magnetic moment distribution ($\lambda = \alpha_{x,y} = \delta_x = 0$, $\delta_z \neq 0$ case)

Here we show the anisotropic Berry curvature and magnetic moment distribution in k space away from the gap opening, using the six-band description (SBD) we developed (see Fig. 6). The formula for calculating Berry curvature and moment distribution are

$$\Omega_n(\mathbf{k}) = 2 \,\mathrm{Re} \sum_{n' \neq n} \frac{i \langle n|\partial H/\partial k_x|n'\rangle \langle n'|\partial H/\partial k_y|n\rangle}{(\varepsilon_n - \varepsilon_{n'})^2}, \quad (A29)$$

$$m_n^{\mathrm{int}}(\mathbf{k}) = \frac{e}{\hbar} \mathrm{Re} \sum_{n' \neq n} \frac{i \langle n|\partial H/\partial k_x|n'\rangle \langle n'|\partial H/\partial k_y|n\rangle}{\varepsilon_n - \varepsilon_{n'}}, \quad (A30)$$

where $n = \{\tau\xi\}$ is the short-hand form, and H is the full six-band Hamiltonian.

5. Nonlinear anomalous Hall effect

Just as $m_n^{\mathrm{int}}(\mathbf{k})$ discussed in the main text gives rise to ME, $\Omega_n(\mathbf{k})$ in the bands enable $1T'$-WTe$_2$ to exhibit a quantum nonlinear Hall effect at zero magnetic field. This can be seen under general symmetry considerations [7]. For the convenience of the reader, we outline this symmetry analysis for a 2D system that only has in-plane mirror symmetry (e.g., $1T'$-WTe$_2$). The nonlinear Hall current can be written as $j_a = \chi_{abb} E_b E_b$ ($a, b = x, y$). Under the operation $(x, y) \rightarrow (x, -y)$, we have $(j_x, j_y) \rightarrow (j_x, -j_y)$ and $(E_x, E_y) \rightarrow (E_x, -E_y)$. This allows a nonzero χ_{xyy} (while χ_{yxx} vanishes). Under an in-plane dc electric field, χ_{xyy} can
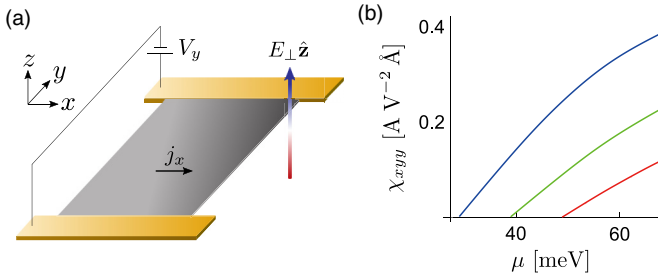
FIG. 7. (a) Schematic of a $1T'$-WTe$_2$ monolayer under a perpendicular electric field $E_\perp \hat{\mathbf{z}}$ and an in-plane electric field E_y, which can give rise to a nonlinear Hall current j_x. (b) Calculated nonlinear Hall conductivity χ_{xyy} (blue) from Eq. (A31) using $\tau = 50$ fs. Parameters used for the pristine part are the same as those in Fig. 1; for the electric-field-induced part, we used α, λ, $\delta_x = 0$, and $\delta_z = 0.075$ eV (blue), 0.05 eV (green), and 0.025 eV (red).

be obtained using [7]

$$\chi_{xyy} = \frac{\tau}{2}\frac{e^3}{\hbar^2}\sum_{n,\mathbf{k}} f^{(0)}_{n\mathbf{k}}\,\partial_{k_y}\Omega_n(\mathbf{k}), \qquad (\text{A31})$$

where τ is the transport scattering time. Similar to Eq. (6) above, $\Omega_n(\mathbf{k})$ is an odd function of k_y [see Fig. 6(a)]. As a result, nonzero χ_{abb} only occurs when $a = x$ and $b = y$: only the electric field along y induces a nonlinear Hall effect along x. When $\mathbf{E}$ is parallel to the x direction, the nonlinear Hall effect (as well as the kinetic ME effect) vanishes.

To illustrate the quantum nonlinear Hall effect, we numerically integrate Eq. (A31) to obtain a finite nonlinear

Hall current conductivity χ_{xyy} in Fig. 7(b) using a scattering time $\tau = 50$ fs. Similar to M_z in the main text, we used the SBD description in order to capture the full reciprocal space distribution of the Berry curvature. This nonlinear Hall conductivity can be probed in a conventional Hall bar measurement (Fig. 7) and provides a fully electrical way of mapping the Berry curvature (dipole).

6. Unitary transformation and form of the Hamiltonian

We note that the model in the supplement of Ref. [1] is equivalent to our model for the pristine part. For the convenience of the reader, we reproduce the four-band Hamiltonian in Ref. [1] as

$$H_F = \begin{pmatrix} \epsilon_c & 0 & -iv_xk_x & v_yk_y \\ 0 & \epsilon_c & v_yk_y & -iv_xk_x \\ iv_xk_x & v_yk_y & \epsilon_v & 0 \\ v_yk_y & iv_xk_x & 0 & \epsilon_v \end{pmatrix}. \qquad (\text{A32})$$

To see the equivalence, we use the unitary transformation

$$U = \frac{1}{\sqrt{2}}\begin{pmatrix} 1 & 1 & 0 & 0 \\ 1 & -1 & 0 & 0 \\ 0 & 0 & i & i \\ 0 & 0 & i & -i \end{pmatrix}. \qquad (\text{A33})$$

Applying the unitary transformation, we have

$$U^\dagger H_F U = \tilde{h}_q, \qquad (\text{A34})$$

reproducing Eq. (A13).

[1] X. F. Qian, J. W. Liu, L. Fu, and L. Li, Science **346**, 1344 (2014).

[2] S. J. Tang *et al.*, Nat. Phys. **13**, 683 (2017).

[3] Z. Y. Fei *et al.*, Nat. Phys. **13**, 677 (2017).

[4] S. F. Wu, V. Fatemi, Q. D. Gibson, K. Watanabe, T. Taniguchi, R. J. Cava, and P. J. Herrero, Science **359**, 76 (2018).

[5] H. T. Yuan *et al.*, Nat. Phys. **9**, 563 (2013).

[6] D. Xiao, W. Yao, and Q. Niu, Phys. Rev. Lett. **99**, 236809 (2007).

[7] I. Sodemann and L. Fu, Phys. Rev. Lett. **115**, 216806 (2015).

[8] J. Lee, Z. F. Wang, H. C. Xie, K. F. Mak, and J. Shan, Nat. Mater. **16**, 887 (2017).

[9] D. MacNeill, G. M. Stiehl, M. H. D. Guimaraes, R. A. Buhrman, J. Park, and D. C. Ralph, Nat. Phys. **13**, 300 (2017).

[10] H. Kurebayashi, Nat. Phys. **13**, 209 (2017).

[11] See the Appendix for discussions of the six-band $\mathbf{k} \cdot \mathbf{p}$ description and symmetry analysis, reduction to a 4×4 effective Hamiltonian, Berry curvature at the band edge, Berry curvature and magnetic moments for nonzero $\delta_z \neq 0$ distribution in momentum space, and the quantum nonlinear anomalous Hall effect.

[12] D. H. Choe, H. J. Sung, and K. J. Chang, Phys. Rev. B **93**, 125109 (2016).

[13] X. Q. Lin and J. Ni, Phys. Rev. B **95**, 245436 (2017).

[14] S.-Y. Xu *et al.*, Nat. Phys. **14**, 900 (2018).

[15] B. A. Bernevig, T. L. Hughes, and S.-C. Zhang, Science **314**, 1757 (2006).

[16] G. L. Bir and G. E. Pikus, *Symmetry and Strain-Induced Effects in Semiconductors* (Wiley, New York, 1974).

[17] R. Winkler, *Spin-Orbit Coupling Effects in Two-Dimensional Electron and Hole Systems* (Springer, Berlin, 2003).

[18] S. A. Tarasenko, M. V. Durnev, M. O. Nestoklon, E. L. Ivchenko, J. W. Luo, and A. Zunger, Phys. Rev. B **91**, 081302 (2015).

[19] D. G. Rothe, R. W. Reinthaler, C. X. Liu, L. W. Molenkamp, S. C. Zhang, and E. M. Hankiewicz, New J. Phys. **12**, 065012 (2010).

[20] L. Muechler, A. Alexandradinata, T. Neupert, and R. Car, Phys. Rev. X **6**, 041069 (2016).

[21] D. Xiao, M. C. Chang, and Q. Niu, Rev. Mod. Phys. **82**, 1959 (2010).

[22] W. Eerenstein, N. D. Mathur, and J. F. Scott, Nature (London) **442**, 759 (2006).

[23] L. S. Levitov, Y. V. Nazarov, and G. M. Eliashberg, Sov. Phys. JETP **61**, 133 (1985).

[24] C. Şahin, J. Rou, J. Ma, and D. A. Pesin, Phys. Rev. B **97**, 205206 (2018).

[25] R. Winkler and U. Zülicke, Phys. Rev. B **82**, 245313 (2010).

[26] M. Zhou, R. Zhang, J. P. Sun, W. K. Lou, D. Zhang, W. Yang, and K. Chang, Phys. Rev. B **96**, 155430 (2017).